

# A $K$ -Band Portable FMCW Radar With Beamforming Array for Short-Range Localization and Vital-Doppler Targets Discrimination

Zhengyu Peng, *Student Member, IEEE*, Lixin Ran, and Changzhi Li, *Senior Member, IEEE*

**Abstract**—This paper presents a printed circuit board realization of a  $K$ -band portable frequency-modulated continuous-wave radar transceiver with beamforming array for short-range localization. The transmitter channel of the proposed radar consists of a free-running voltage-controlled oscillator (VCO) and a single patch antenna. A linear frequency-modulated chirp signal is generated by the VCO, which is controlled by an analog “sawtooth” voltage generator. The receiver channel has a four-element linear beamforming array, a six-port circuit, and a baseband circuit. The beam of the array can be continuously steered in a range of  $\pm 45^\circ$  on the  $H$ -plane through an array of vector controllers. Each vector controller is capable of simultaneously controlling the phase and the amplitude of the corresponding array element. The design principle of the binary-phase-shift attenuator, the vector controller, and the radar system are discussed. Calibration method of the array is introduced to minimize the errors caused by component variation and fabrication. The radiation patterns of the array with phase-only beam steering and phase-amplitude beamforming are measured and compared, demonstrating the advantage of the beamforming design. System-level experiments showed that the proposed solution is suitable for short-range localization. In addition, experiments with a human subject revealed the capability of the proposed radar system to discriminate a human target from other objects based on the vital-Doppler effect.

**Index Terms**—Beamforming array, continuous beam steering, frequency-modulated continuous-wave (FMCW) radar, localization, vector controller.

## I. INTRODUCTION

APPLICATIONS of radar systems have been extended to commercial areas, such as driver assistance [1], [2], industrial localizations [3], through-wall detections [4], [5], and biomedical applications [6]–[8]. Typically, mechanical steering system or phased array is necessary for a radar system to perform a 2-D or 3-D scan. It is known that mechanical

steering systems increase the size, weight, and cost while limiting the reliability. For consumer electronics, the size of the system is usually essential in order to be mounted on existing devices and equipment, such as automobiles and medical instrument, without affecting their profiles and functions. Phased array radar systems, which feature lightweight, low profile, and high steering speed [9], overcome the drawbacks of mechanical beam steering systems. However, a conventional phased array is expensive, especially at frequencies above the  $K$ -band. This is mainly because conventional solutions require high-frequency phase shifters, which have a limited number of manufacturers and are expensive. New beamforming techniques are emerging for higher frequencies. One of the simplest approaches to realize beam steering at frequencies above 24 GHz is using delay methods and radio-frequency (RF) switches [10]–[12]. However, these methods usually have limited number of steering angles, and the signal routing will be troublesome with an increasing number of steering angles. Other techniques, such as current-reused active phase shifting [13], local oscillator (LO) phase shifting [14], [15], and vector modulator [16], [17], are based on solid-state circuits. The LO phase-shifting technique requires a complex multiphase voltage-controlled oscillator (VCO) and multiple phase select switches. Its steering angles are also discrete. The vector modulator technique based on the concept of vector sum [18]–[20], which features continuous phase and amplitude control, is a good alternative to high-frequency phase shifters.

Regarding radar systems, continuous-wave (CW) radars have the advantage of low transmit power, simple structure, and high sensitivity, which enable wide applications in various areas. The frequency-modulated continuous-wave (FMCW) radar is one of the most popular CW radar types [21]–[24] with the ability to obtain absolute range information. Transceiver architecture based on six-port [25] features, simple structure, and high performance, and has been used in biomedical interferometry radars [26], [27] and FMCW radars [28], [29].

In this paper, a  $K$ -band portable FMCW radar with beamforming array is proposed. To the best of the authors' knowledge, this is the first printed circuit board (PCB) realization of short-range localization radar with beamforming capability in  $K$ -band. The proposed radar system includes both the transmitter and receiver channels. The transmitter channel consists of a VCO and a single patch antenna. A “sawtooth”

Manuscript received November 18, 2016; revised January 23, 2017; accepted January 27, 2017. Date of publication February 17, 2017; date of current version September 1, 2017. This work was supported in part by the NSF under Grant ECCS-1254838 and Grant 61528104.

Z. Peng and C. Li are with the Department of Electrical and Computer Engineering, Texas Tech University, Lubbock, TX 79409 USA (e-mail: zhengyu.peng@ttu.edu; changzhi.li@ttu.edu).

L. Ran is with the Laboratory of Applied Research on Electromagnetics, Zhejiang University, Hangzhou 310027, China (e-mail: ranlx@zju.edu.cn).

Color versions of one or more of the figures in this paper are available online at <http://ieeexplore.ieee.org>.

Digital Object Identifier 10.1109/TMTT.2017.2662680

0018-9480 © 2017 IEEE. Personal use is permitted, but republication/redistribution requires IEEE permission.

See [http://www.ieee.org/publications\\_standards/publications/rights/index.html](http://www.ieee.org/publications_standards/publications/rights/index.html) for more information.

voltage generated by an operational-amplifier-based circuit is used to control the VCO to generate a frequency-modulated RF signal from 23.5 to 24 GHz. The receiver channel consists of a beamforming array, a six-port circuit, and a baseband circuit. The beamforming array is a four-element linear array. Each element is a series-fed microstrip patch array antenna. The beam of the array can be continuously steered with a range of  $\pm 45^\circ$  on the  $H$ -plane through an array of vector controllers. The vector controller is based on the concept of vector sum [18], [19]. However, different from previous works [18]–[20] that are based on either integrated circuits or bulky modules, this design realizes the concept in  $K$ -band by simple microwave structure and p-i-n diodes on a PCB. Each vector controller is capable of controlling the phase and the amplitude of the corresponding array element of the four-element linear array. The beat signal of the FMCW radar is detected by the six-port circuit and then sampled by the soundcard of a laptop. The whole radar system is fabricated on PCB. Characteristics of the vector controller are measured. As PCB implementation of a  $K$ -band system inevitably suffers from errors due to component variation, mismatch, soldering, and fabrication errors, a calibration method is proposed and experimentally demonstrated as effective.

The proposed solution will be implemented on a Rogers RO3006 laminate. The radiation patterns of the beamforming array will be measured to confirm that the proposed system can form more complex beam patterns since the vector controller can simultaneously control both the phase and amplitude of  $K$ -band signals. In system level measurement, the advantage of beamforming with lower side lobes to minimize ghost images for localization will be demonstrated. Finally, an experiment will demonstrate the radar system has a high motion sensing sensitivity to capture the vital-Doppler effect and discriminate living targets from stationary targets.

This paper will be organized as follows. Section II will present the design principle of the proposed radar system. In Section III, experiments will be performed to demonstrate the calibration procedure for the beamforming array, and the patterns of the beamforming array steered to different angles will be measured. Section IV will present experiments that demonstrate the advantages of the proposed radar system for short-range localization. Finally, a conclusion will be drawn in Section V.

## II. DESIGN PRINCIPLE

This section presents the design principle for the proposed radar system. Fig. 1 illustrates the top-level block diagram of the proposed radar system. In the transmitter channel, a “sawtooth” voltage sequence is generated by the “sawtooth” generator [28], [30]. This “sawtooth” voltage sequence is used to control a free-running VCO to generate a frequency-modulated RF signal. Half of this signal is transmitted by a transmitter antenna and the other half is used as a LO to drive the six-port circuit. Regarding the receiver channel, the beamforming array receives the signal reflected by targets. Then a six-port circuit is used to detect the beat signal, which is processed by a baseband circuit and sampled by the soundcard

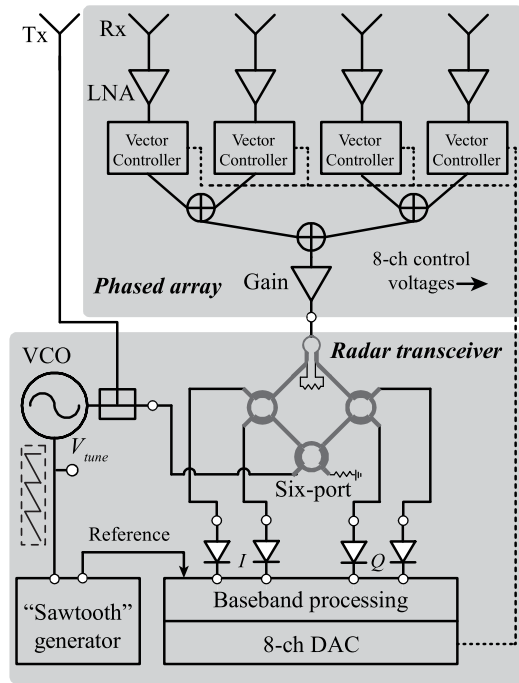


Fig. 1. Top-level block diagram of the proposed radar system with beamforming array.

of a laptop. The beamforming array is a four-element linear array. The beam of the array can be continuously steered on the  $H$ -plane through an array of vector controllers. The vector controllers are controlled by an eight-channel DAC, which is driven by a data acquisition device (DAQ) through a serial peripheral interface (SPI) bus.

The baseband signal processing method has been reported in [28] and [30]. A reference pulse sequence is used to align the phase of each beat signal and maintain the coherence of radar system.

### A. Beamforming Array

Typically, in a transceiver system, an array can be implemented in either the transmitter or the receiver. For beamforming array designed in this paper, if it is used in the transmitter, the RF amplifiers used in the array should be able to handle relatively high power levels (above 0 dBm) in order to maintain enough transmit power. In this case, the linearity requirement for the RF amplifiers is difficult to be satisfied, especially in  $K$ -band. Therefore, this work has a single patch antenna on the transmitter side and an array on the receiver side.

The beamforming array in the proposed radar system is designed to be steerable on the  $H$ -plane and fixed on the  $E$ -plane on the receiver channel. The fundamental theory of the proposed beamforming array is based on the authors' previous work [31]. The proposed beamforming array in this radar system is a four-element linear array. The distance between adjacent elements is  $\lambda/2$ . Each array element is a three-element series-fed microstrip patch array antenna. Fig. 2 demonstrates one channel of the proposed beamforming array, which has a three-element series-fed microstrip patch array, a low-noise amplifier (LNA), and a vector controller cascaded

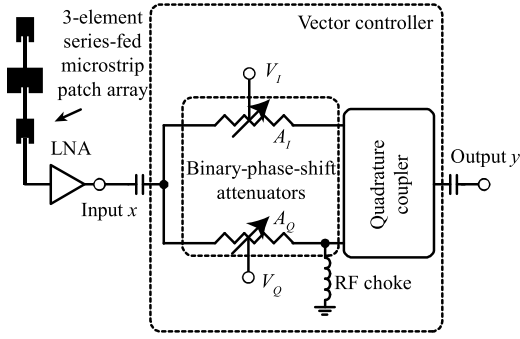
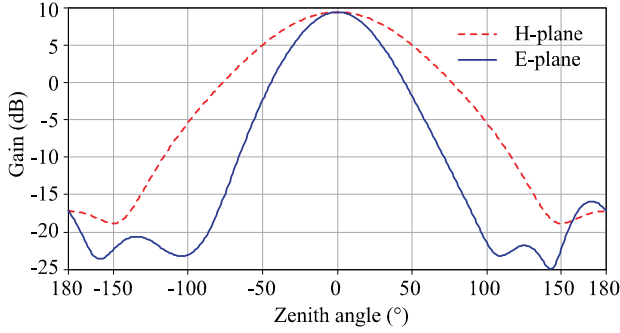


Fig. 2. One channel of the beamforming array.

Fig. 3. Simulated *H*-plane and *E*-plane patterns of a three-element series-fed microstrip patch array.

in sequence. The vector controller has a pair of binary-phase-shift attenuators, a power divider, and a quadrature coupler.

1) *Antenna*: The three-element series-fed microstrip patch array antenna is designed with a narrow beamwidth on the *E*-plane and a wide beamwidth on the *H*-plane. Fig. 3 shows the simulated patterns of the *H*-plane and the *E*-plane. The gain of the single three-element series-fed microstrip patch array is 9.41 dB. The beamwidth on the *E*-plane is 48.6°, and the beamwidth on the *H*-plane is 81.5°.

2) *Binary-Phase-Shift Attenuator*: The binary-phase-shift attenuator is the key component in the vector controller. The schematic of the binary-phase-shift attenuator is illustrated in Fig. 4(a). The attenuator is designed based on a quadrature coupler, which has two p-i-n diodes terminating ports *b* and *c*, respectively, with proper matching structures and bias circuits. Ports *a* and *d* are the input and output ports, respectively. The relation of the reflected voltage waves, incident voltage waves and the *S*-parameter matrix of an ideal quadrature coupler can be written as

$$\begin{bmatrix} V_a^- \\ V_b^- \\ V_c^- \\ V_d^- \end{bmatrix} = \begin{bmatrix} S_{aa} & S_{ab} & S_{ac} & S_{ad} \\ S_{ba} & S_{bb} & S_{bc} & S_{bd} \\ S_{ca} & S_{cb} & S_{cc} & S_{cd} \\ S_{da} & S_{db} & S_{dc} & S_{dd} \end{bmatrix} \begin{bmatrix} V_a^+ \\ V_b^+ \\ V_c^+ \\ V_d^+ \end{bmatrix} \quad (1)$$

where  $S_{ab} = S_{ba} = S_{cd} = S_{dc} = -j/\sqrt{2}$ ,  $S_{ac} = S_{ca} = S_{bd} = S_{db} = -1/\sqrt{2}$ , and  $S_{aa} = S_{bb} = S_{cc} = S_{dd} = S_{ad} = S_{da} = S_{cd} = S_{dc} = 0$ .  $V^-$  is the reflected voltage wave at each port, and  $V^+$  is the incident voltage wave of the corresponding port. Based on the connection shown in Fig. 4(a), the reflection coefficient of an ideal p-i-n diode is  $\Gamma = V_b^+/V_b^- = V_c^+/V_c^-$ .

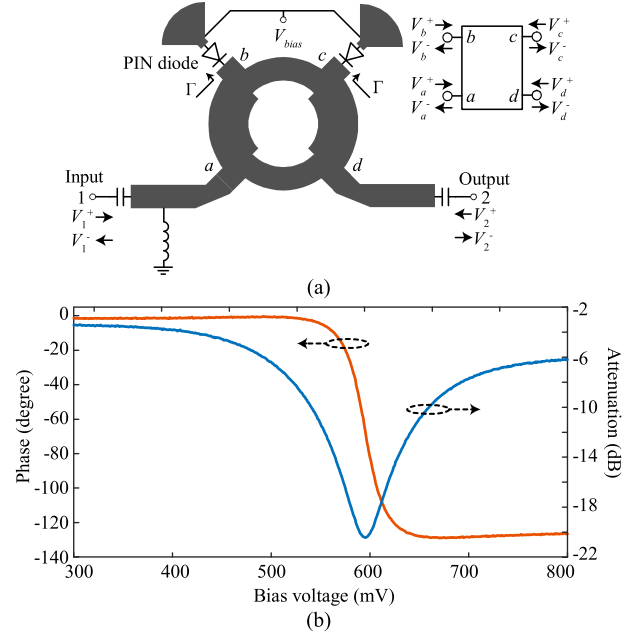


Fig. 4. (a) Schematic of the binary-phase-shift attenuator. (b) Measured amplitude and phase response to different bias voltages.

The *S*-parameter matrix of the binary-phase-shift attenuator can be expressed as

$$\begin{bmatrix} V_1^- \\ V_2^- \end{bmatrix} = \begin{bmatrix} V_a^- \\ V_d^- \end{bmatrix} = \begin{bmatrix} S_{11} & S_{12} \\ S_{21} & S_{22} \end{bmatrix} \begin{bmatrix} V_a^+ \\ V_d^+ \end{bmatrix} = S_{\text{atten}} \begin{bmatrix} V_1^+ \\ V_2^+ \end{bmatrix} \quad (2)$$

where  $S_{\text{atten}}$  is the *S*-parameter matrix of the attenuator. Combining (1) and (2), the *S*-parameter of the attenuator can be derived as

$$S_{11} = S_{22} = \frac{V_1^-}{V_1^+} = \frac{-jV_b^+ - V_c^+}{\sqrt{2}V_1^+} \quad (3)$$

$$S_{21} = S_{12} = \frac{V_2^-}{V_1^+} = \frac{\Gamma(-V_b^+ - jV_c^+)}{jV_b^+ - V_c^+} = j\Gamma. \quad (4)$$

For an ideal quadrature coupler,  $V_c^+ = -jV_b^+$ , thus,  $S_{11} = S_{22} = 0$ , i.e., the input and output of the attenuator are matched. The attenuation and phase shift of the attenuator are

$$|S_{21}| = |\Gamma| \quad (5)$$

$$\angle S_{21} = \pi/2 + \pi \text{sign}(\Gamma)/2. \quad (6)$$

It is known that the resistance of an ideal p-i-n diode varies according to its forward bias current and can range from 0  $\Omega$  to hundreds of  $\Omega$ . Thus the reflection coefficient  $\Gamma$  of an ideal p-i-n diode, without considering parasitics, varies from  $-1$  to  $1$ . According to (5), When the resistance is 50  $\Omega$ ,  $\Gamma = 0$  for a 50  $\Omega$  system, which results in the maximum attenuation from port 1 to port 4.

From (6), there are two phase states for this attenuator, i.e.,  $0^\circ$  and  $180^\circ$ , achieving binary phase shift required for the proposed vector controller. However, parasitics and PCB fabrication errors introduce an error between the binary phase states. For example, Fig. 4(b) is the measured results of a prototype binary-phase-shift attenuator at 23.75 GHz with bias voltage increasing from 300 to 800 mV. A phase difference of

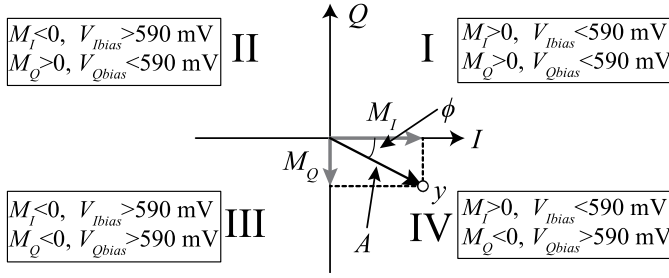


Fig. 5. Distribution of the output signal on a constellation diagram.

130° is achieved for the binary phase states, and the attenuation ranges from −4 to −20 dB.

### B. Vector Controller

The block diagram of the vector controller is shown in Fig. 2. The input RF signal is divided into two channels, and each channel has a binary-phase-shift attenuator, which has two phase states, i.e., 0° and 180°. After the attenuators, these two channels are combined with a quadrature coupler. DC block capacitors and bias circuits are added to control the bias currents of the p-i-n diodes.

For an input signal  $x = \sin(2\pi f_c t)$  passing through the vector controller, the output  $y$  can be written as

$$\begin{aligned} y &= M_I \sin(2\pi f_c t) + M_Q \cos(2\pi f_c t) \\ &= \text{Re}\{Ae^{j\phi}e^{-j2\pi f_c t}\} \end{aligned} \quad (7)$$

where  $f_c$  is the carrier frequency,  $M_I = \pm A_I/2$  and  $M_Q = \pm A_Q/2$ , with  $A_I, A_Q$  being the attenuations of the two attenuators. The signs of  $M_I$  and  $M_Q$  are determined by the phase states of the two attenuators, i.e.,  $M_I$  and  $M_Q$  are positive when the phase state is 0°, and are negative when the phase state is 180°. As shown in Fig. 5, the output  $y$  can be mapped to the constellation diagram. The radius  $A$  between point  $y$  and the origin in Fig. 5 is the output amplitude, and the angle  $\phi$  is the output phase shift

$$A = \sqrt{M_I^2 + M_Q^2} \quad (8)$$

$$\phi = \arctan \frac{M_Q}{M_I}. \quad (9)$$

Based on the characteristic of the binary-phase-shift attenuator, the output distribution of the vector controller related to the bias voltages can be marked in Fig. 5. The output signal  $y$  is distributed in all the four quadrants, which means it is possible to adjust the phase and amplitude simultaneously by changing the bias voltages of the attenuators, and the phase-shift range is 360°.

A prototype of the vector controller has been designed and fabricated, as shown in Fig. 6. The substrate of the PCB is Rogers RO3006 with a thickness of 0.254 mm. The p-i-n diode used in the prototype is Skyworks SMP1302, whose parasitic capacitance is smaller than 0.03 pF. The board is 15 mm × 43 mm.

Measured results of the prototype at 23.75 GHz are shown in Fig. 7. Each point in the constellation diagram represents a  $S_{21}$  result at certain control voltages  $V_I$  and  $V_Q$ . The voltage sweep

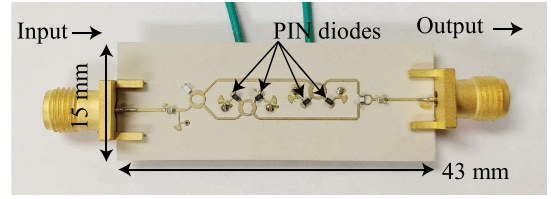


Fig. 6. Photograph of the vector controller prototype.

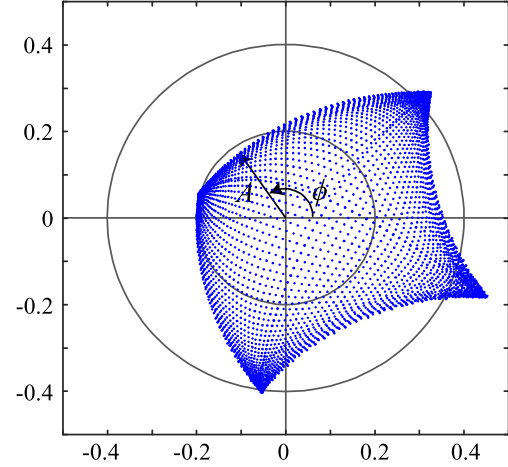


Fig. 7. Measured constellation diagram of the vector controller at 23.75 GHz (voltage swept between 300 and 800 mV with a 5-mV step for both attenuators).

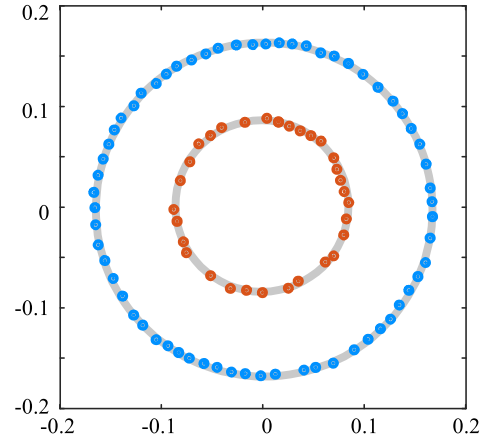


Fig. 8. Two concentric circles extracted from Fig. 7.

range for both attenuators is between 300 and 800 mV with a 5-mV step size. For every single point in the constellation diagram, the radius  $A$  corresponds to the attenuation of the vector controller in linear scale, and the angle  $\phi$  represents the phase shift of the vector controller. Since the points are distributed in all the four quadrants, the phase-shift range of the proposed vector controller can reach to 360°. The measured results match with the analysis.

Fig. 8 shows two circles extracted from Fig. 7. Each circle has a different constant attenuation. The function of the vector controller in each circle is identical to a simple phase shifter, which has a 360° phase-shift range. By simply modifying the bias voltages, more concentric circles can be extracted from Fig. 7, which means 0° to 360° phase shifts with different

TABLE I  
PERFORMANCE COMPARISON WITH RECORDED WORKS

Reference	[32]	[33]	[34]	This work
Frequency (GHz)	22	24	22.5	<b>23.75</b>
Technology	0.18 $\mu\text{m}$ CMOS	0.18 $\mu\text{m}$ CMOS	0.13 $\mu\text{m}$ CMOS	<b>PCB</b>
Operation type	Continuous	Continuous	Continuous	<b>Continuous</b>
Control voltage (V)	-0.5 --- 0.8	-1.4 --- 1	1.4 --- 3.0	<b>0.3 --- 0.8</b>
Phase range (degree)	336	360	136	<b>360</b>
Minimal insertion loss (dB)	14.7	10.1	10.5	<b>10</b>

attenuations can be obtained, thus achieving simultaneous phase and amplitude control.

Table I compares published *K*-band phase shifter [32]–[34] with the proposed work. Almost all the realizations of *K*-band phase shifters in the literature are based on monolithic techniques. However, this work is based on PCB, with  $360^\circ$  phase tuning range and 10- to 60-dB tunable insertion loss.

### C. FMCW Radar

As shown in Fig. 1, a free-running VCO controlled by  $V_{\text{tune}}$  generates a *K*-band frequency-modulated RF signal [28], which is transmitted by a single patch antenna. The same *K*-band frequency-modulated RF signal also drives a six-port circuit to down-convert the received signal and obtains the differential quadrature baseband signal. Design considerations for the parameters of the six port can be found in the literature [35], [36]. The VCO control voltage  $V_{\text{tune}}$  is generated by a pair of operational amplifiers. A reference signal generated at the same time with the  $V_{\text{tune}}$  voltage is used to align the phase of each beat signal detected by the FMCW radar, thus keeping the radar system coherent. A soundcard from a laptop is used to acquire the baseband beat signal as well as the reference signal. The line-in mode of the soundcard is used, so that the soundcard can acquire two channels at the same time. One channel of the soundcard is for the reference signal; the other channel is for either the *I* or *Q* channel of the baseband output from the down-converter. As FMCW radars do not require quadrature demodulation, one channel of the *I/Q* baseband output is sufficient to obtain the target range information. The edges of each beat signal, which are affected by the receiver signal's return time and the falling edge of the "sawtooth" voltage should be blanked. The blanking method is illustrated in Fig. 9. The chirp repetition period is  $T_c = 8$  ms, resulting in 1536 samples for every beat signal with a 192 ks/s sampling rate. Since our design is for short-range applications within 20 m, the corresponding receiver signal's return time ( $T_d < 0.13 \mu\text{s}$ ) is much shorter than the sample period of  $5.2 \mu\text{s}$ . Thus, the major contribution of the edge distortion is due to the falling edge ( $T_f = 1$  ms) of the "sawtooth"

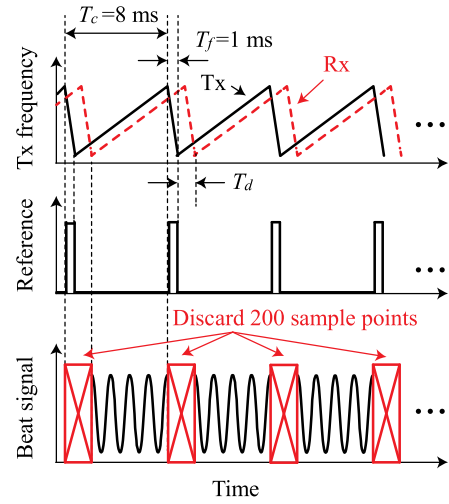


Fig. 9. Beat signal edge blanking (drawn not to scale).

voltage, and this edge distortion can be easily eliminated by discarding the first 200 samples at the beginning of each beat signal. The beginning of each beat signal is determined by the reference signal generated from the same circuit, which is sampled together with the beat signal. All the signal processing procedures, including aligning the phase of each beat signal, are accomplished in real time in the laptop.

### D. Vital-Doppler Effect for Living Targets

Micro-Doppler has been used to characterize human gaits and differentiate moving human targets with other animals [37], [38]. For a stationary living target, such as a human subject who is sitting or standing still, it is also possible to discriminate it from other stationary objects based on the vital-Doppler effect. The vital-Doppler effect is caused by physiological motions, such as respiration of a living target, which will slightly change the radar cross section of the target and cause a variation in the amplitude of the radar-detected range spectrum at the range bins corresponding to the living target. By analyzing the variation of the range spectrum detected by the proposed FMCW radar system, living targets can be localized. Moreover, the electronic beamforming array makes it possible for the radar system to discriminate the stationary living target among other targets in a large area without mechanically turning the radar.

## III. ARRAY CALIBRATION AND PATTERN MEASUREMENT

In order to control the phase of each array element, there are two typical methods to obtain the relations among the phase shift  $\phi$ , the attenuation  $A$ , and the control voltages, i.e.,  $V_I$  and  $V_Q$ . The first method is using a polynomial to fit the curves in Fig. 4(b), which seems to be easy to execute but is not reliable due to fabrication errors, component variations, and soldering variations for a PCB-level implementation in the *K*-band. The other method relies on a calibration procedure to establish a lookup table, which can minimize the errors caused by fabrication, component variations, and soldering variations.



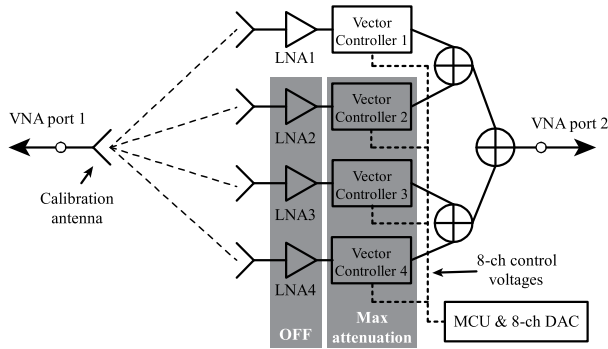


Fig. 10. Experiment setup of beamforming array calibration.

### A. Array Calibration

Array calibration requires a vector network analyzer (VNA) and a calibration antenna, denoted as “probe antenna” henceforth. In the setup, the calibration antenna and the beamforming array are placed face to face. The calibration procedure is described as follows.

- 1) Turn on all the four LNAs and tune the eight control voltages to get the minimum magnitude of  $S_{21}$ , which means each vector controller is in the “maximum attenuation” state. Record the value of each control voltage.
- 2) Since the lengths of microstrip lines in different channels are designed to be the same, the signal phase delay from the receiver antennas to port 2 of the VNA is the same for each channel in the initial state (with LNAs turned on and  $V_I = V_Q = 0$ ). As a result, the phase of each channel can be recorded in the initial state.
- 3) Obtain the relative phase shift as a function of control voltages for each individual channel. The relative phase shift is obtained by comparing the instant phase shift with that measured in the initial state. In this step, the LNAs of other channels are turned off and the vector controllers of the other channels are in the maximum attenuation state. Fig. 10 shows the configuration when calibrating channel 1.

It should be noted that this calibration method minimizes errors introduced by fabrications, component variations, and soldering variations. However, there are still residual errors, due to factors such as unequal phase delays in the initial state. The coupling between adjacent antennas will also introduce phase shift. Despite these errors, the proposed calibration method minimizes the dominating uncertainty in controlling the beamforming array.

### B. Beam Steering With Phase Control Only

Experiments have been taken to measure the far-field patterns of the beamforming array with different steering angles by changing the phase shift of the vector controllers. Fig. 11 shows the measurement environment in a microwave anechoic chamber. The distance between the beamforming array and the standard horn antenna was about 1 m. During the experiment, the beamforming array was turned from  $-90^\circ$  to  $90^\circ$  with a  $3^\circ$  step on a turntable.

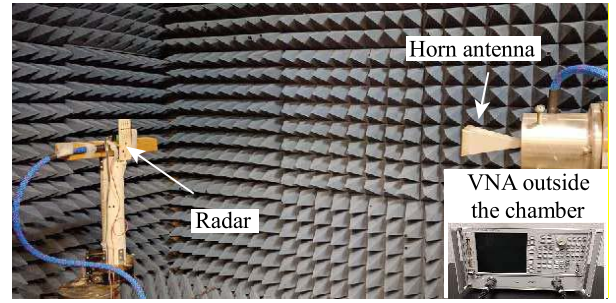


Fig. 11. Experiment environment of the pattern measurement for the beamforming array. Inset: VNA outside the chamber.

TABLE II  
CONTROL VOLTAGES TO OBTAIN THE PATTERNS IN FIG. 12

Angle	Channel 1		Channel 2		Channel 3		Channel 4	
	$V_I$ (mV)	$V_Q$ (mV)	$V_I$ (mV)	$V_Q$ (mV)	$V_I$ (mV)	$V_Q$ (mV)	$V_I$ (mV)	$V_Q$ (mV)
$-45^\circ$	550	521	635	609	525	600	567	510
$-30^\circ$	550	521	640	570	595	630	520	590
$-15^\circ$	550	521	594	515	635	566	630	610
$0^\circ$	550	521	535	500	540	515	546	515
$15^\circ$	550	521	365	590	515	597	556	620
$30^\circ$	550	521	490	588	595	630	635	565
$45^\circ$	550	521	528	620	640	577	530	530

The measured patterns of the beamforming array steered to different angles are illustrated in Fig. 12. Patterns with seven different angles, i.e.,  $-45^\circ$ ,  $-30^\circ$ ,  $-15^\circ$ ,  $0^\circ$ ,  $15^\circ$ ,  $30^\circ$ , and  $45^\circ$ , were plotted at the frequency of 23.75 GHz. The corresponding control voltages to obtain the seven patterns are listed in Table II.

It can be observed in Fig. 12 that at angles of  $-45^\circ$  and  $45^\circ$ , the side lobes of the patterns are comparable with the main lobes, which will introduce ghost images for radar applications.

Regarding the bandwidth of the beamforming array, the measured patterns of the array steered to  $-15^\circ$  at different frequencies are illustrated in Fig. 13. The patterns of the beamforming array at frequencies of 23.5, 23.75, and 24 GHz are consistent, which means the proposed beamforming array has a bandwidth from 23.5 to 24 GHz.

### C. Beamforming With Phase and Amplitude Control

As discussed in Section II, the vector controller can tune the phase and amplitude at the same time. Thus, advanced beamforming methods, such as nulling array and beam broadening [20], [39], can be achieved with the proposed radar system.

In this paper, an example of beam steering with different amplitude weights is used to demonstrate the flexibility of beamforming. In this example, the amplitude weights of the four array elements are 0.5, 1, 1, and 0.5, respectively, which can achieve measured radiation patterns as shown in Fig. 14. The steering directions were tuned to  $-45^\circ$ ,  $-30^\circ$ ,  $-15^\circ$ ,  $0^\circ$ ,  $15^\circ$ ,  $30^\circ$ , and  $45^\circ$ . Compared with Fig. 12, which used

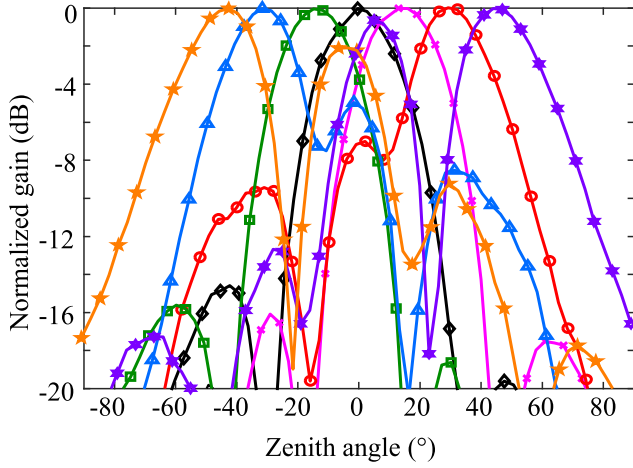


Fig. 12. Measured patterns of the phased array steered to  $-45^\circ$ ,  $-30^\circ$ ,  $-15^\circ$ ,  $0^\circ$ ,  $15^\circ$ ,  $30^\circ$ , and  $45^\circ$  at 23.75 GHz with phase-only beam steering.

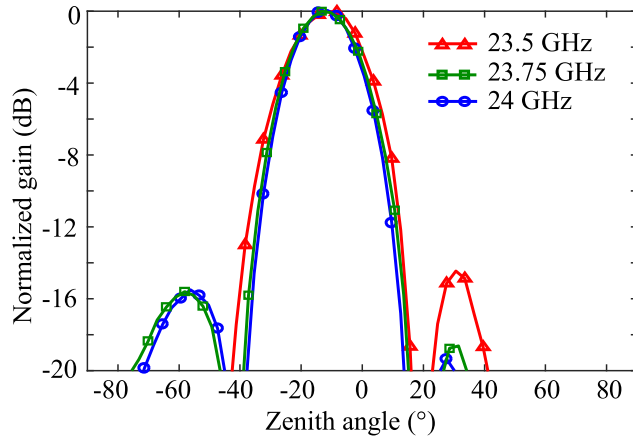


Fig. 13. Measured patterns when the phased array is steered to  $-15^\circ$  at different frequencies.

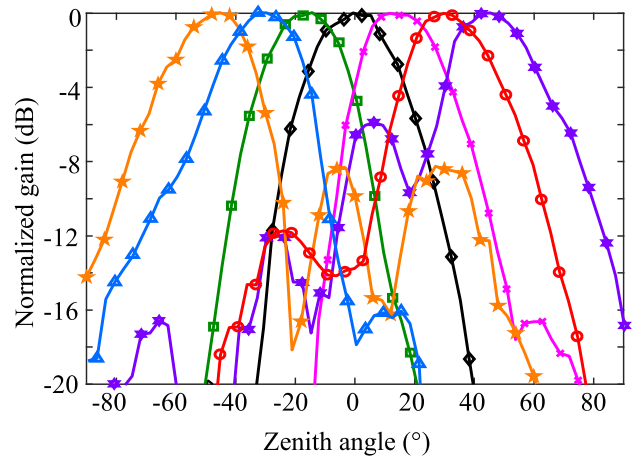


Fig. 14. Measured patterns of the beamforming array steered to  $-45^\circ$ ,  $-30^\circ$ ,  $-15^\circ$ ,  $0^\circ$ ,  $15^\circ$ ,  $30^\circ$ , and  $45^\circ$  at 23.75 GHz with phase and amplitude beamforming.

phase control only to tune the steering directions, the side lobes of the patterns obtained by simultaneous phase and amplitude control were significantly lowered. However, their beamwidth were broadened as a tradeoff. The corresponding

TABLE III  
CONTROL VOLTAGES TO OBTAIN THE PATTERNS IN FIG. 14

Angle	Channel 1		Channel 2		Channel 3		Channel 4	
	$V_I$ (mV)	$V_Q$ (mV)	$V_I$ (mV)	$V_Q$ (mV)	$V_I$ (mV)	$V_Q$ (mV)	$V_I$ (mV)	$V_Q$ (mV)
$-45^\circ$	560	535	663	630	490	620	575	539
$-30^\circ$	560	535	680	575	600	662	545	580
$-15^\circ$	560	535	600	473	665	565	610	592
$0^\circ$	560	535	510	445	523	485	560	539
$15^\circ$	560	535	380	535	475	605	565	604
$30^\circ$	560	535	373	600	600	662	610	564
$45^\circ$	560	535	495	643	675	585	547	545

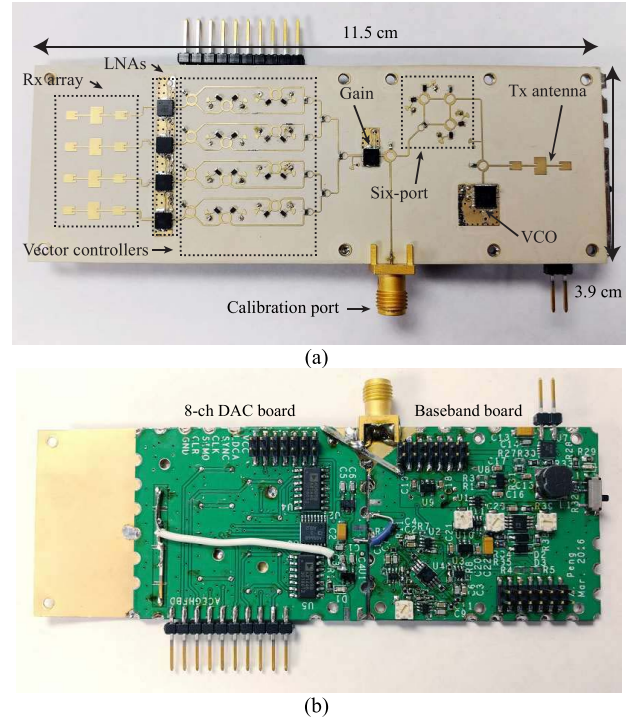


Fig. 15. Photographs of the proposed radar prototype. (a) Top view. (b) Bottom view.

control voltages to obtain the five patterns are listed in Table III.

#### IV. RADAR SYSTEM EXPERIMENT

Experiment with the proposed radar system has been performed in a short-range localization demonstration. Fig. 15 is the photograph of the proposed radar system. The entire radar prototype has a size of  $11.5 \text{ cm} \times 3.9 \text{ cm}$  and weighs 69 g. The substrate material used for the RF board is Rogers RO3006, and the substrate material for the baseband board is FR4. Table IV lists the main components used in the radar prototype. In the beamforming array, the LNAs are MACOM MAAL-011111, and the p-i-n diodes are Skyworks SMP1302. In the FMCW radar transceiver part, the VCO is Analog Devices HMC739LP4, the gain block is MACOM MAAL-011111, and the Schottky diodes are Skyworks SMS7621-040LF. The main

TABLE IV  
LIST OF COMPONENTS OF THE PROPOSED RADAR SYSTEM

Radar Part	Device	Manufacturer	Function
Beamforming array	MAAL-011111	MACOM	LNA
	SMP1302	Skyworks	PIN diode
FMCW transceiver	HMC739LP4	Analog Devices	VCO
	MAAL-011111	MACOM	LNA
	SMS7621	Skyworks	Schottky diode
Baseband	ADA4851	Analog Devices	OpAmp
	AD5668	Analog Devices	DAC

TABLE V  
LIST OF COMPONENTS OF THE PROPOSED RADAR SYSTEM

Tx power	8 dBm	Rx voltage gain	56 dB
Tx bandwidth	500 MHz	Center frequency	23.75 GHz
Chirp repetition period	8 ms	Baseband sampling rate	192 ksps
Range resolution	0.3 m	Power consumption	1.93 W

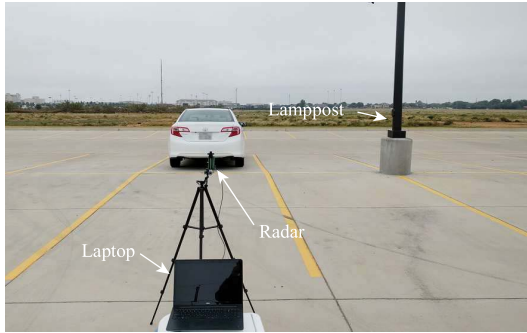


Fig. 16. Experimental environment of short-range localization with two targets using the proposed radar prototype.

components in the baseband are the operational amplifiers (Analog Devices ADA4851) and the DAC (Analog Devices AD5668). The DAC is driven by the National Instruments USB-DAQ through a SPI bus. Detailed parameters of the radar system are listed in Table V.

#### A. Object Targets

The short-range localization experimental setup is shown in Fig. 16. A car and a lamppost were in the radar's field of view. The scanning angle of the radar started from  $-45^\circ$  to  $45^\circ$  with a step size of  $2.5^\circ$ . The radar system was powered by a single 9 V battery. The first measurement was performed with phase-only beam steering, and the result is illustrated in Fig. 17. Another measurement was performed with phase and amplitude beamforming, which was discussed in Section III.

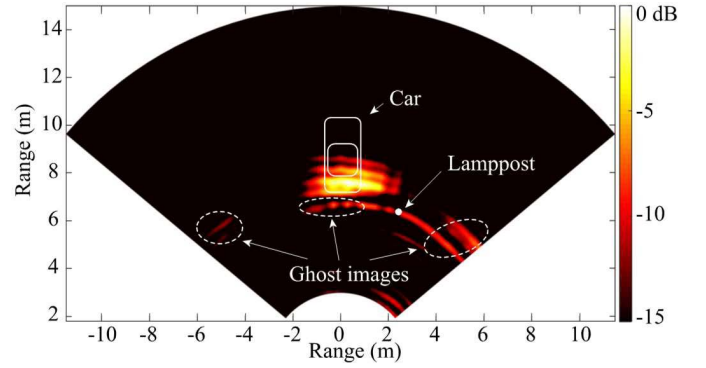


Fig. 17. Measured result of the short-range localization experiment using the proposed radar prototype with phase-only beam steering.

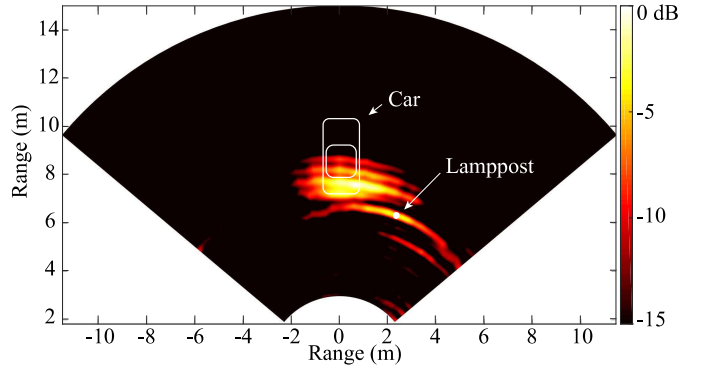


Fig. 18. Experimental environment of short-range localization using the proposed radar prototype with phase and amplitude beamforming.



Fig. 19. Experimental environment of short-range localization with a human subject and two object targets using the proposed radar prototype.

The result is shown in Fig. 18. In both results, the signatures of the car and the lamppost are present. Comparing the two measurement results, ghost images can be observed in Fig. 17, which was caused by the large side lobes of the phase-only beam steering. On the other hand, in Fig. 18, the ghost images are much weaker than the ones in Fig. 17. However, it suffered from worse angular resolution, which was caused by the beam broadening effect of the adopted beamforming method.

#### B. Stationary Human Target and Object Targets

In the second experiment, a human subject stood in front of the car and the lamppost, as shown in Fig. 19. The scanning



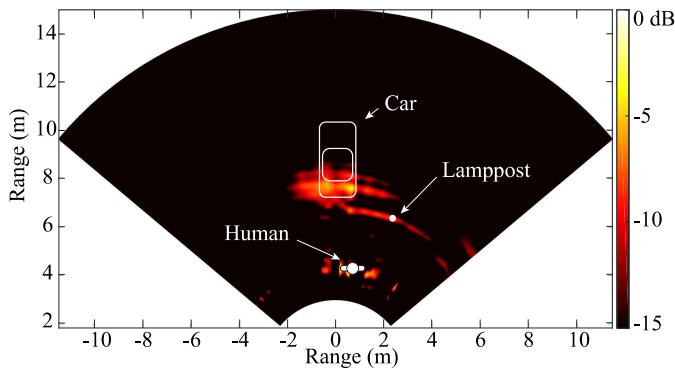


Fig. 20. Measured result of the short-range localization experiment with a human subject and two object targets using the proposed radar prototype.

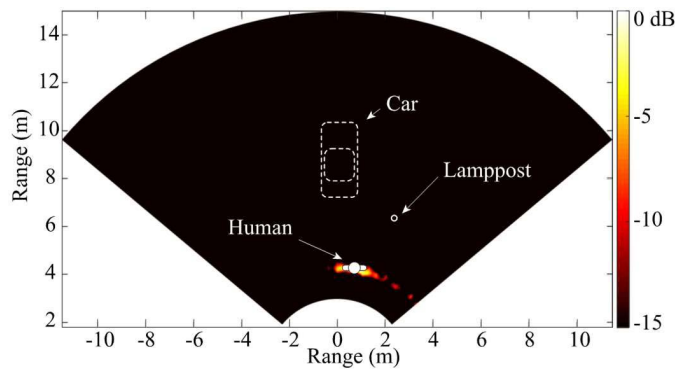


Fig. 21. Human target extracted with standard deviation of ten sequencing scans.

angle also started from  $-45^\circ$  to  $45^\circ$  with a step size of  $2.5^\circ$ . In this measurement, the phase and amplitude beamforming method was used. Fig. 20 illustrates the measured result. Signatures of the car, the lamppost, and the human subject can be clearly seen. It should be noted that the signature of the human subject is not consistent, because of the vital-Doppler effect. To identify the human subject, ten sequences of FMCW scans were performed and the standard deviation of the detected range spectrum is drawn in Fig. 21. With this method, the signatures of the car and the lamppost are suppressed and the human signature can be extracted, achieving human-aware localization.

## V. CONCLUSION

A PCB realization of a K-band portable FMCW radar with beamforming array is presented in this paper. It demonstrated an alternative approach to achieve portable and low-cost beamforming array radar systems with vector controllers and a six-port circuit. Array patterns steered to different directions were measured. In addition, complex beamforming that utilizes both phase shift and amplitude weight of the array was realized. Two localization experiments were carried out. The first one with two stationary objects demonstrated that the system is suitable for short-range localization with an electrical beam scanning range of  $\pm 45^\circ$ . The second one revealed the capability of the system to discriminate stationary human subjects from other objects based on the vital-Doppler

effect. The proposed work has the potential for multiple applications, including driver assistance, indoor drone and robot navigation, industrial localization, and security surveillance. In addition, with the capability to generate complex radiation patterns, the beamforming array can be easily adopted by other communication and sensing systems.

## ACKNOWLEDGMENT

Authors Z. Peng and C. Li would like to acknowledge Dr. M. Saed and A. Alajmi for their help in measuring the radiation pattern of the beamforming array.

## REFERENCES

- [1] D. M. Grimes and T. O. Jones, "Automotive radar: A brief review," *Proc. IEEE*, vol. 62, no. 6, pp. 804–822, Jun. 1974.
- [2] J. Hatch, A. Topak, R. Schnabel, T. Zwick, R. Weigel, and C. Waldschmidt, "Millimeter-wave technology for automotive radar sensors in the 77 GHz frequency band," *IEEE Trans. Microw. Theory Techn.*, vol. 60, no. 3, pp. 845–860, Mar. 2012.
- [3] M. Vossiek, L. Wiebking, P. Gulden, J. Wiegardt, C. Hoffmann, and P. Heide, "Wireless local positioning," *IEEE Microw. Mag.*, vol. 4, no. 4, pp. 77–86, Dec. 2003.
- [4] F. Ahmad and M. G. Amin, "Noncoherent approach to through-the-wall radar localization," *IEEE Trans. Aerosp. Electron. Syst.*, vol. 42, no. 4, pp. 1405–1419, Oct. 2006.
- [5] E. J. Baranoski, "Through wall imaging: Historical perspective and future directions," in *Proc. IEEE Int. Conf. Acoust., Speech Signal Process.*, Las Vegas, NV, USA, Mar. 2008, pp. 5173–5176.
- [6] C. Li, V. M. Lubecke, O. Boric-Lubecke, and J. Lin, "A review on recent advances in Doppler radar sensors for noncontact healthcare monitoring," *IEEE Trans. Microw. Theory Techn.*, vol. 61, no. 5, pp. 2046–2060, May 2013.
- [7] R. Rotman, "Recent advances using microwaves for imaging, hyperthermia and interstitial ablation of breast cancer tumors," in *Proc. IEEE Int. Conf. Microw., Commun., Antennas Electron. Syst. (COMCAS)*, Tel Aviv, Israel, Nov. 2011, pp. 1–4.
- [8] T. Elmissaoui, N. Soudani, and R. Bouallegue, "UWB radar for medical applications," in *Proc. 12th Int. Radar Symp. (IRS)*, Leipzig, Germany, Sep. 2011, pp. 526–531.
- [9] H. J. Visser, *Array and Phased Array Antenna Basics*. Hoboken, NJ, USA: Wiley, 2006.
- [10] M.-S. Lee and Y.-H. Kim, "Design and performance of a 24-GHz switch-antenna array FMCW radar system for automotive applications," *IEEE Trans. Veh. Technol.*, vol. 59, no. 5, pp. 2290–2297, Jun. 2010.
- [11] W. Lee, J. Kim, and Y. J. Yoon, "Compact two-layer rotman lens-fed microstrip antenna array at 24 GHz," *IEEE Trans. Antennas Propag.*, vol. 59, no. 2, pp. 460–466, Feb. 2011.
- [12] M. Morinaga, T. Nagasaku, H. Shinoda, and H. Kondoh, "24 GHz intruder detection radar with beam-switched area coverage," in *IEEE MTT-S Int. Microw. Symp. Dig.*, Honolulu, HI, USA, Jun. 2007, pp. 389–392.
- [13] H. Jia *et al.*, "A 77 GHz frequency doubling two-path phased-array FMCW transceiver for automotive radar," *IEEE J. Solid-State Circuits*, vol. 51, no. 10, pp. 2299–2311, Oct. 2016.
- [14] H. Hashemi, X. Guan, A. Komijani, and A. Hajimiri, "A 24-GHz SiGe phased-array receiver-LO phase-shifting approach," *IEEE Trans. Microw. Theory Techn.*, vol. 53, no. 2, pp. 614–625, Feb. 2005.
- [15] X. Guan, H. Hashemi, and A. Hajimiri, "A fully integrated 24-GHz eight-element phased-array receiver in silicon," *IEEE J. Solid-State Circuits*, vol. 39, no. 12, pp. 2311–2320, Dec. 2004.
- [16] T. Yu and G. M. Rebeiz, "A 22–24 GHz 4-element CMOS phased array with on-chip coupling characterization," *IEEE J. Solid-State Circuits*, vol. 43, no. 9, pp. 2134–2143, Sep. 2008.
- [17] C.-W. Wang, H.-S. Wu, and C.-K. C. Tzuang, "CMOS passive phase shifter with group-delay deviation of 6.3 ps at K-band," *IEEE Trans. Microw. Theory Techn.*, vol. 59, no. 7, pp. 1778–1786, Jul. 2011.
- [18] P.-Y. Chen, T.-W. Huang, H. Wang, Y.-C. Wang, C.-H. Chen, and P.-C. Chao, "K-band HBT and HEMT monolithic active phase shifters using vector sum method," *IEEE Trans. Microw. Theory Techn.*, vol. 52, no. 5, pp. 1414–1424, May 2004.

- [19] P.-S. Wu, H.-Y. Chang, M.-D. Tsai, T.-W. Huang, and H. Wang, "New miniature 15–20-GHz continuous-phase/amplitude control MMICs using 0.18- $\mu\text{m}$  CMOS technology," *IEEE Trans. Microw. Theory Techn.*, vol. 54, no. 1, pp. 10–18, Jan. 2006.
- [20] Z. Peng *et al.*, "Radio frequency beamforming based on a complex domain frontend," *IEEE Trans. Microw. Theory Techn.*, vol. 64, no. 1, pp. 289–298, Jan. 2016.
- [21] T. Mitomo, N. Ono, H. Hoshino, Y. Yoshihara, O. Watanabe, and I. Seto, "A 77 GHz 90 nm CMOS transceiver for FMCW radar applications," *IEEE J. Solid-State Circuits*, vol. 45, no. 4, pp. 928–937, Apr. 2010.
- [22] S. Scheiblhofer, S. Schuster, and A. Stelzer, "High-speed FMCW radar frequency synthesizer with DDS based linearization," *IEEE Microw. Wireless Compon. Lett.*, vol. 17, no. 5, pp. 397–399, May 2007.
- [23] N. Pohl, T. Jaeschke, and K. Aufinger, "An ultra-wideband 80 GHz FMCW radar system using a SiGe bipolar transceiver chip stabilized by a fractional- $N$  PLL synthesizer," *IEEE Trans. Microw. Theory Techn.*, vol. 60, no. 3, pp. 757–765, Mar. 2012.
- [24] T. Musch, "A high precision 24-GHz FMCW radar based on a fractional- $N$  ramp-PLL," *IEEE Trans. Instrum. Meas.*, vol. 52, no. 2, pp. 324–327, Apr. 2003.
- [25] S. O. Tatu and K. Wu, "Six-port technology and applications," in *Proc. 11th Int. Conf. Telecommun. Modern Satellite, Cable Broadcast. Ser. (TELSIKS)*, vol. 1. Niš, Serbia, Oct. 2013, pp. 239–248.
- [26] G. Vinci *et al.*, "Six-port radar sensor for remote respiration rate and heartbeat vital-sign monitoring," *IEEE Trans. Microw. Theory Techn.*, vol. 61, no. 5, pp. 2093–2100, May 2013.
- [27] G. Vinci *et al.*, "24 GHz six-port medical radar for contactless respiration detection and heartbeat monitoring," in *Proc. 9th Eur. Radar Conf. (EuRAD)*, Amsterdam, The Netherlands, Oct. 2012, pp. 75–78.
- [28] Z. Peng and C. Li, "A portable 24-GHz FMCW radar based on six-port for short-range human tracking," in *Proc. IEEE MTT-S Int. Microw. Workshop Ser. RF Wireless Technol. Biomed. Healthcare Appl. (IMWS-BIO)*, Sep. 2015, pp. 81–82.
- [29] H. Zhang, L. Li, and K. Wu, "Software-defined six-port radar technique for precision range measurements," *IEEE Sensors J.*, vol. 8, no. 10, pp. 1745–1751, Oct. 2008.
- [30] Z. Peng, J.-M. Munoz-Ferreras, Y. Tang, R. Gómez-García, and C. Li, "Portable coherent frequency-modulated continuous-wave radar for indoor human tracking," in *Proc. IEEE Topical Conf. Biomed. Wireless Technol., Netw., Sens. Syst. (BioWireless)*, Austin, TX, USA, Jan. 2016, pp. 36–38.
- [31] Z. Peng, L. Lixin Ran, and C. Li, "A 24-GHz low-cost continuous beam steering phased array for indoor smart radar," in *Proc. IEEE 58th Int. Midwest Symp. Circuits Syst. (MWSCAS)*, Fort Collins, CO, USA, Aug. 2015, pp. 1–4.
- [32] C.-H. Wu, W.-T. Li, J.-H. Tsai, and T.-W. Huang, "Design of a K-band low insertion loss variation phase shifter using 0.18- $\mu\text{m}$  CMOS process," in *Proc. IEEE Asia-Pacific Microw. Conf.*, Dec. 2010, pp. 1735–1738.
- [33] J.-C. Wu, C.-C. Chang, S.-F. Chang, and T.-Y. Chin, "A 24-GHz full-360° CMOS reflection-type phase shifter MMIC with low loss-variation," in *Proc. IEEE Radio Freq. Integr. Circuits Symp.*, Jun. 2008, pp. 365–368.
- [34] A. B. Nguyen and J.-W. Lee, "A K-band CMOS phase shifter MMIC based on a tunable composite metamaterial," *IEEE Microw. Wireless Compon. Lett.*, vol. 21, no. 6, pp. 311–313, Jun. 2011.
- [35] S. Linz *et al.*, "I/Q imbalance compensation for six-port interferometers in radar applications," in *Proc. 44th Eur. Microw. (EuMC)*, Rome, Italy, Oct. 2014, pp. 746–749.
- [36] A. Stelzer, C. G. Diskus, and R. Weigel, "Accuracy considerations and FMCW operation of a six-port device," in *Proc. Asia-Pacific Microw. Conf. (APMC)*, vol. 2, Dec. 2001, pp. 407–410.
- [37] S. S. Ram and H. Ling, "Analysis of microDopplers from human gait using reassigned joint time-frequency transform," *Electron. Lett.*, vol. 43, no. 23, p. 1, Nov. 2007.
- [38] M. Otero, "Application of a continuous wave radar for human gait recognition," *Proc. SPIE*, vol. 5809, pp. 538–548, May 2005.
- [39] Z. Peng, T. Hu, W. Cui, J. Huangfu, C. Li, and L. Ran, "Unconventional beamforming for quasi-hemispheric coverage of a phased array antenna," *IEEE Antennas Wireless Propag. Lett.*, vol. 12, pp. 1654–1657, Dec. 2013.



**Zhengyu Peng** (S'15) received the B.S. and M.Sc. degrees in electrical engineering from Zhejiang University, Hangzhou, China, in 2011 and 2014, respectively. He is currently pursuing the Ph.D. degree in electrical engineering at Texas Tech University, Lubbock, TX, USA.

His current research interests include antennas, microwave circuits, and biomedical applications of microwave/RF circuits and systems.

Mr. Peng was a recipient of the 2016 IEEE Microwave Theory and Techniques Society Graduate Fellowship and the Excellent Demo Track Presentation Award in 2016 IEEE Radio and Wireless Week. He won Third Place of the Student Design Competition for high sensitivity radar in the 2015 IEEE MTT-S International Microwave Symposium. He is a Reviewer for the IEEE TRANSACTIONS ON CIRCUITS AND SYSTEMS—II: EXPRESS BRIEFS and the *International Journal of Electronics and Communications*.



**Lixin Ran** received the B.S., M.S., and Ph.D. degrees from Zhejiang University, Hangzhou, China, in 1991, 1994, and 1997, respectively.

He was with the Department of Information and Electronics Engineering, Zhejiang University, where he became an Assistant Professor in 1997, an Associate Professor in 1999, and a Full Professor in 2004. In 2005, 2009, and 2012, he was with the Massachusetts Institute of Technology, as a Visiting Scientist. He is currently the Director of the Laboratory of Applied Research on Electromagnetics,

Zhejiang University. He has co-authored over 120 research papers published in peer-reviewed journals and is the inventor of over 30 licensed patents. His current research interests include new concept antennas, radio-aware sensing and imaging, radio frequency, microwave and terahertz systems, and artificial active media.



**Changzhi Li** (S'06–M'09–SM'13) received the B.S. degree in electrical engineering from Zhejiang University, Hangzhou, China, in 2004, and the Ph.D. degree in electrical engineering from the University of Florida, Gainesville, FL, USA, in 2009.

During 2007–2009, he was with Alereon Inc., Austin, TX, USA, and Coherent Logix Inc., Austin, where he was involved with ultra-wideband transceivers and software-defined radio. In 2009, he joined Texas Tech University, Lubbock, TX, USA, as an Assistant Professor and became an Associate

Professor in 2014. His current research interests include biomedical applications of microwave/RF, wireless sensor, and analog circuits.

Dr. Li was a recipient of the ASEE Frederick Emmons Terman Award in 2014, the IEEE-HKN Outstanding Young Professional Award in 2014, the NSF Faculty Early CAREER Award in 2013, and the IEEE MTT-S Graduate Fellowship Award in 2008. He was the recipient of several Best Paper Awards as an author/advisor in IEEE-sponsored conferences. He served as the TPC Co-Chair of the IEEE Wireless and Microwave Technology Conference in 2012 and 2013. He served as an Associate Editor of the IEEE TRANSACTIONS ON CIRCUITS AND SYSTEMS—II: EXPRESS BRIEFS in 2014 and 2015. He is an Associate Editor of the IEEE TRANSACTIONS ON CIRCUITS AND SYSTEMS—I: REGULAR PAPERS.